FISEVIER

Contents lists available at ScienceDirect

Surface & Coatings Technology

journal homepage: www.elsevier.com/locate/surfcoat





Phase transition zones in compositionally complex alloy films influenced by varying Al and Ti content

Daniel C. Goodelman^a, Danielle E. White^b, Andrea M. Hodge^{a,b,*}

- a Department of Aerospace and Mechanical Engineering, University of Southern California, 3650 McClintock Ave. Los Angeles, CA 90089, USA
- b Department of Chemical Engineering and Materials Science, University of Southern California, 925 Bloom Walk, HED 216, Los Angeles, CA 90089, USA

ARTICLE INFO

Keywords: Magnetron sputtering Compositionally complex alloys (CCAs) Nanoindentation Microstructural characterization

ABSTRACT

Phase changes due to compositional variation of alloying elements in the AlCrFeNiTi and AlCoFeNiTi families of compositionally complex alloys (CCAs) were investigated by employing magnetron co-sputtering synthesis techniques and microstructural characterization via scanning electron microscopy, X-ray diffraction, and energy dispersive X-ray spectroscopy. Compositional alterations were introduced by varying the input power provided to either an Al or Ti target, as well as by the substrate quadrant location. A synergistic relationship between Al and Ti was observed in which both elements compete to drive phase formation, and was revealed to be further influenced by substituting Cr with similarly sized, but structurally dissimilar, Co. The crystallinity of the studied samples was mapped with respect to Ti and Al content to emphasize the distinct compositions where phase transitions occur for each CCA family. Nanoindentation was employed to study how different phases affect the mechanical properties, with results indicating that amorphous samples generally exhibited lower hardness and moduli when compared to the crystalline and "mixed" phase samples. This work highlights how sputtering can be used to control individual elements within CCA families in order to examine how their atomic characteristics contribute to phase formation and crystallinity.

1. Introduction

The study of multi-principal element alloys (MPEAs), a field including high entropy alloys (HEAs) and compositionally complex alloys (CCAs), has been an exciting topic of novel alloy development. MPEAs feature a variety of desirable properties, including high hardness and strength [1-4], fatigue resistance [5,6], fracture toughness [7], biocompatibility [8], resistance to oxidation [9,10], wear [3,11-13], and corrosion [14-17], and have been shown to exhibit unique electrical and magnetic properties [18-21]. To date, the emphasis of the field has focused on the development of HEAs, however, CCAs present the opportunity to explore a larger composition space due to a more flexible alloy definition. While both HEAs and CCAs are composed of four or more alloying elements between 5 and 35 at.% of the total composition, such that there is no base element, HEAs are commonly equiatomic and the term "HEA" is typically used when either the configurational entropy or the objective of producing single-phase solid solutions is important [22]. In comparison, CCAs do not need to be equiatomic and can possess crystal structures other than single-phase solid solutions [23]. Traditional synthesis methods to fabricate bulk CCAs include spark plasma sintering [24], mechanical alloying [25] and arc melting [26], though such techniques have demonstrated a lack of control over grain size, global composition and elemental distribution [27], and possess limitations in high-throughput screening within the vast composition space of CCAs [28].

In contrast, techniques such as physical vapor deposition (PVD) present a high-throughput alternative for CCA synthesis, allowing for the exploration of multiple compositions, and/or compositional gradients on the same substrate [29–31]. Current experimental works have indicated that CCA films and coatings exhibit comparable mechanical and physical properties to their bulk counterparts, which range from high hardness to unique magnetic properties [32–38]. However, differences in growth mechanisms, grain size, process temperature, and rapid diffusion during synthesis can contribute to discrepancies in phase formation between bulk and thin film studies [39]. For example, CCA film synthesis via PVD features rapid cooling rates compared to bulk CCA synthesis methods [40], which can restrict diffusion and minimize the nucleation and growth of intermetallic compounds, ultimately

E-mail addresses: goodelma@usc.edu (D.C. Goodelman), dewhite@usc.edu (D.E. White), ahodge@usc.edu (A.M. Hodge).

^{*} Corresponding author at: Department of Chemical Engineering and Materials Science, University of Southern California, 925 Bloom Walk, HED 216, Los Angeles, CA 90089, USA.

inhibiting phase separation [41]. Additionally, the influence of alloying elements, such as Al [9,29,42,43], Cu [44–46], Ni [46], V [11], and Ti [13,47], have been documented in bulk arrangements, but their impact on thin film morphology has yet to be thoroughly explored.

To date, the preferred processing method for deposited MPEA films has been magnetron sputtering [40,48,49] with a focus primarily on nitride and oxide-films [34–36,38,48,50–53]. The wide range of tunable conditions [49] in sputtering include the ability to deposit nearly any single element, alloy, or ceramic material, as well as tailorable deposition parameters such as working pressure, working gas, and target power [54]. Sputtering from a single MPEA target with a set composition has been employed in many systems [32,37,39,55-62]; however, stoichiometry control can be further enhanced by leveraging co-sputtering assemblies and depositing from multiple targets. This technique allows for the ability to change the deposition rate of individual target materials and thus contributes to compositional variation and microstructural development [40]. Additionally, co-sputtering enables individual elements within the MPEA arrangement to be isolated, granting the opportunity to focus on their atomic characteristics including atomic size, crystallography, and valence electron structure, all which contribute to phase formation within these materials. In general, experimental studies that have varied elemental compositions within MPEA systems treat alloy synthesis as a pseudo-binary arrangement dictated by the Hume-Rothery rules [63] with a single "large" element and several "small" elements. Herein, "large" element refers to those with an atomic radii greater than 140 pm, while the remaining "small" elements are usually transition metals with similar atomic radii of approximately 130 pm or less. In those cases, the "large" element typically drives phase formation mechanisms, as it greatly contributes to atomic size differences and lattice distortion effects [40]. However, both the synthesis method (as outlined previously) and electron structure of the "large" element cause inconsistencies in phase formation across studies. Furthermore, studies beyond one "large" element or the influence of the smaller elements have been limited specifically within the context of phase formation.

In this study, magnetron co-sputtering techniques were employed to vary the composition of two "large" elements (Al and Ti) within the AlCrFeNiTi and AlCoFeNiTi CCA families to examine their influence on

Table 1 Elemental composition derived from EDS data for systems 1 and 2 in the AlCr-FeNiTi family.

			AlCrFeNiTi	•		
System	Sample	Al (at. %)	Ti (at. %)	Cr (at. %)	Fe (at. %)	Ni (at. %)
1	S1-7Al-T	7.05	12.81	26.10	26.58	27.47
	S1-7Al-B	7.64	19.31	23.90	24.19	24.89
	S1-15Al-	15.12	18.76	21.62	21.94	22.57
	T					
	S1-15Al-	15.08	12.68	23.86	23.84	24.54
	В					
	S1-33Al-	32.42	14.66	17.32	17.45	18.15
	T					
	S1-33Al-	32.75	10.47	18.42	18.74	19.62
	В					
2	S2-5Ti-T	16.60	5.00	25.71	25.66	27.04
	S2-5Ti-B	26.58	5.17	22.33	22.56	23.36
	S2-7Ti-T	17.24	6.32	25.37	24.96	26.11
	S2-7Ti-B	26.52	6.73	21.80	22.10	22.86
	S2-8Ti-T	14.45	7.66	25.67	25.58	26.63
	S2-8Ti-B	23.05	8.12	22.50	22.48	23.86
	S2-13Ti-	23.54	12.69	20.95	21.01	21.81
	T					
	S2-13Ti-	15.60	12.08	23.79	23.86	24.66
	В					
	S2-32Ti-	19.85	32.12	15.76	15.76	16.51
	T					
	S2-32Ti-	13.34	31.74	18.04	18.33	18.55
	В					

phase morphology transitions. Additionally, Cr was substituted with similarly sized, but structurally dissimilar, Co to observe the effect of the "small" elements on the overall microstructure. Respective compositions are maintained between 5 and 35 at.% in accordance with the defined CCA range. The resultant microstructures were characterized using scanning electron microscopy (SEM), energy dispersive X-ray spectroscopy (EDS), and X-ray diffraction (XRD) techniques to determine crystallite size and critical alloying element composition thresholds where crystallographic transitions could occur. The mechanical properties, namely hardness and moduli, were examined using nanoindentation to correlate structural trends to compositional variations. Overall, this study highlights phase transitions in sputtered materials while simultaneously exploring the contributions of both "large" and "small" elements in compositionally complex arrangements, which can serve as model alloy systems for future CCA design.

2. Materials & methods

Samples were synthesized using direct current (DC) magnetron sputtering from high purity, single element Al (99,99%) and Ti (99.995%) targets, as well as vacuum arc melted ternary alloy CrFeNi (99.9%) and CoFeNi (99.9%) targets (Plasmaterials, Inc.). A threesource sputtering configuration was used to co-sputter both of the single element targets with one of the ternary alloy targets onto 50 mm Si (100) substrates to produce ${\sim}1~\mu m$ thick AlCrFeNiTi and AlCoFeNiTi films. The working distance for all targets was 13 cm. Each substrate was separated into quadrants to synthesize multiple compositional arrangements simultaneously with the assistance of masking and a pneumatic shutter (see Fig. S1 and description in the Supplementary materials). Due to the orientation of the setup, two distinct sputtering runs can be completed per substrate, yielding four unique compositions. These sputtering conditions are included in Tables SI and SII in the Supplementary materials. Sputtering powers were selected such that the nominal expected composition values for each alloying element were within the necessary defined range for CCAs. The resulting sample thicknesses were measured using an AMBiOS XP-2 profilometer. It should be noted that the nomenclature for the samples presented in this study is separated into "systems" and individual sample names. The systems are as follows: within the AlCrFeNiTi family, system 1 (varied Al) and system 2 (varied Ti); within the AlCoFeNiTi family, system 3 (varied Al) and system 4 (varied Ti). Each individual sample is labeled with the system number, the composition of the varied element in at.%, and the sputtering quadrant region on the substrate i.e., either top (T) or bottom (B). For example, S1-5Al-T constitutes the sample within system 1 with 5 at.% Al from the top quadrant, while S2-32Ti-B corresponds to a sample within system 2 with a 32 at.% Ti from the bottom quadrant.

The elemental compositions of each sample were characterized by scanning electron microscopy/energy dispersive X-ray spectroscopy (SEM/EDS) (FEI Helios G4 P-FIB) at 15 kV. Top-surface micrographs were acquired via SEM using a beam current of 50 pA and an accelerating voltage of 10 kV. Grazing incidence X-ray diffraction (GIXRD) with Cu K α radiation and a grazing angle of 2° was employed. Scans were conducted over a 2θ range from 20° to 120° or to 140° depending on the system of samples, with a step size of 0.05° /sec and a sampling rate of 1° /min using a Rigaku Ultima IV Diffractometer. Average crystallite size was determined from the full-width half maximum (FWHM) of the main diffraction peaks using Sherrer's Equation [64], presented in Eq. (1):

$$t = \frac{0.9\lambda}{B\cos\theta_B} \tag{1}$$

where t is the crystallite size, λ is the X-ray wavelength, B is the FWHM of the peak, and θ_B is the Bragg angle. In addition to microstructural characterization, nanoindentation was performed in a Hysitron Triboindenter with a 50 nm Berkovich tip using a force-controlled, constant loading rate load function. A set of 100 indents, positioned 20 μ m apart

 $\begin{tabular}{ll} \textbf{Table 2} \\ \textbf{Elemental composition derived from EDS data for systems 3 and 4 in the} \\ \textbf{AlCoFeNiTi family.} \\ \end{tabular}$

			AlCoFeNiT	i		
System	Sample	Al (at. %)	Ti (at. %)	Co (at. %)	Fe (at. %)	Ni (at. %)
3	S3-5Al-T	5.75	13.08	25.76	27.61	27.81
	S3-5Al-B	6.47	19.63	23.51	24.82	25.57
	S3-10Al-	9.43	12.12	24.91	26.56	26.98
	T					
	S3-10Al-	10.42	19.39	22.52	23.91	23.75
	В					
	S3-30Al-	29.61	10.44	19.09	20.26	20.61
	T					
	S3-30Al-	30.54	15.29	18.36	17.19	18.63
	В					
4	S4-5Ti-T	11.39	3.93	28.55	27.01	29.21
	S4-5Ti-B	17.32	4.25	24.83	26.63	26.97
	S4-9Ti-T	9.65	8.84	25.99	27.72	27.89
	S4-9Ti-B	15.43	9.34	23.86	25.66	25.72
	S4-35Ti-	7.91	32.10	19.31	20.40	20.28
	T					
	S4-35Ti-	12.06	34.34	17.95	17.42	18.24
	В					

in the center of each sample quadrant, were measured to derive hardness and reduced elastic moduli values. The equation for reduced modulus is provided in Eq. (2) [65]:

$$E_r = \frac{S\sqrt{\pi}}{2\sqrt{A}}\tag{2}$$

where E_r is the reduced modulus, S is the stiffness of the unloading curve, and A is the contact area. Representative load-displacement curves are included in the Supplementary materials (Figs. S2 and S3).

3. Results & discussion

As previously mentioned, there is limited research of CCA arrangements beyond those which are comprised of a single "large" element amongst several "small" elements largely due to synthesis control limitations [28]. However, a versatile synthesis technique like magnetron sputtering affords the ability to isolate each individual element ("large" or "small"), while elucidating on how atomic characteristics contribute to phase formation. In this study, sputtering allowed for the synthesis of four unique compositions per substrate, as outlined in the Materials & methods section (Section 2). Alterations in composition were introduced depending on which element was varied (Al or Ti) and the substrate

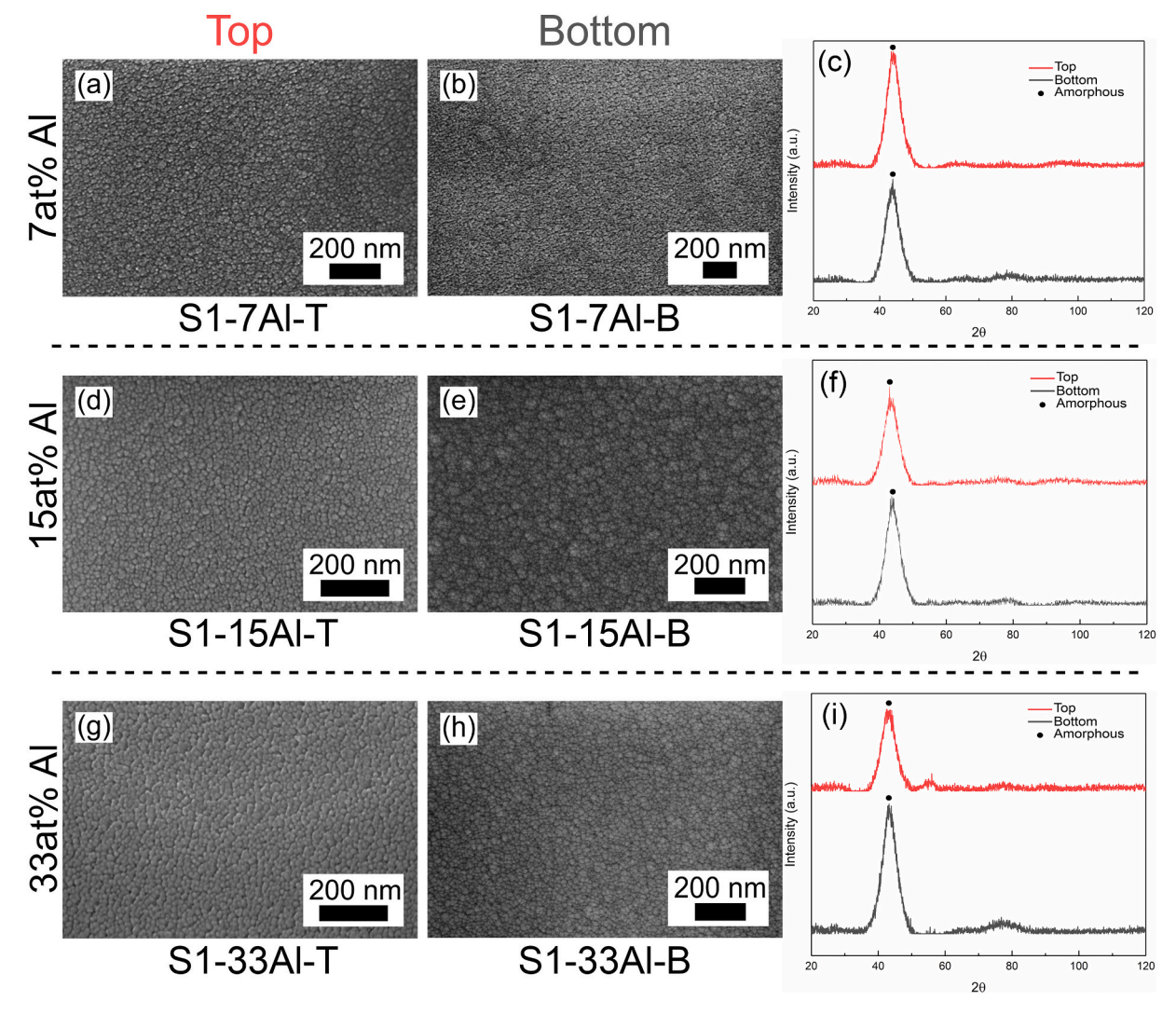


Fig. 1. Varied Al in AlCrFeNiTi family (System 1) - top surface SEM micrographs (a, b, d, e, g, and h) and diffractograms (c, f, and i). Each row represents samples with the same Al content (7, 15, and 33 at.% respectively). Columns are split amongst samples that were in either the "top" or "bottom" substrate quadrant position during the sputtering process, while diffractograms are color-coded based on that position.

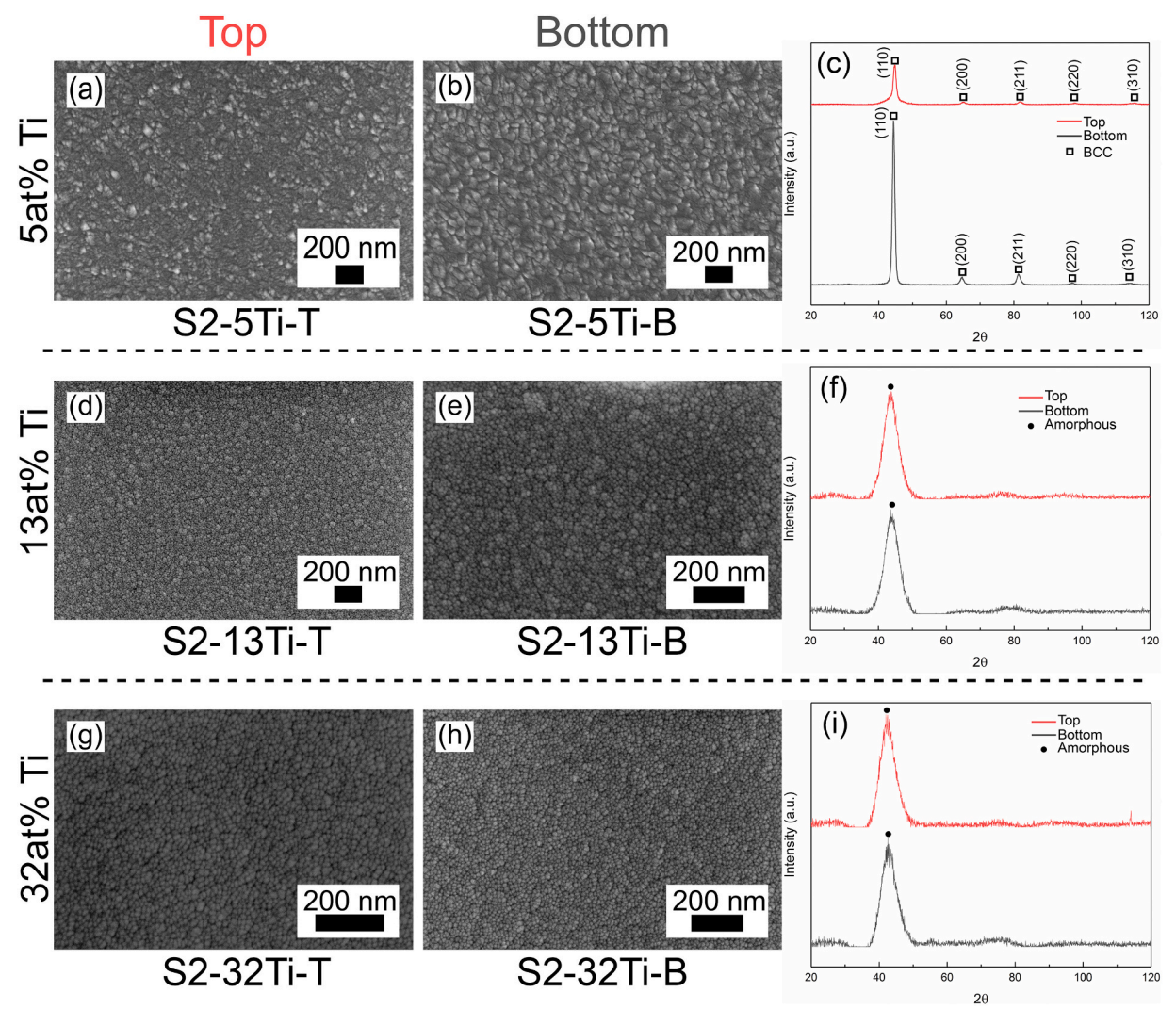


Fig. 2. Varied Ti in AlCrFeNiTi family (system 2) - top surface SEM micrographs (a, b, d, e, g, and h) and diffractograms (c, f, and i). Each row represents samples with the same Ti content (5, 13, and 32 at.% respectively). Columns are split amongst samples that were in either the "top" or "bottom" substrate quadrant position during the sputtering process, while diffractograms are color-coded based on that position.

quadrant position of the sample (either top or bottom). These compositional values are presented in Tables 1 and 2. As such, the role of having multiple "large" elements in a CCA arrangement is explored by varying the Al and Ti content in the AlCrFeNiTi (Section 3.1) and AlCoFeNiTi (Section 3.2) families, while simultaneously exploring the influence of "small" elements i.e., Cr vs. Co. Average crystallite sizes for all samples are included in Table SIII in the Supplementary materials*. Section 3.3 further explores the effect of composition on mechanical properties by using nanoindentation techniques.

3.1. AlCrFeNiTi - the role of multiple "large" elements

System 1 in this study explores the effects of varying the Al content on the overall CCA composition and crystal structure within the AlCr-FeNiTi family. Fig. 1 highlights top surface SEM micrographs and corresponding XRD patterns for all samples within system 1, where each row depicts a distinct Al composition (7 at.%, 15 at.%, and 33 at.%). As seen in the SEM micrographs, all samples in system 1 feature nanocrystallites with roughly the same size (\sim 1.6 nm, see Table SIII*), shape, and orientation, where limited microstructural variations are observed with changes in Al composition. This is also reflected in the XRD scans provided in Fig. 1c, f, and i, which show a single amorphous peak for each of the samples. Since all samples within system 1 are amorphous

regardless of Al content, it is possible that the other alloying elements are driving the phase formation. For example, previous literature has stated that there is a critical Ti content which could lead to the formation of an amorphous phase in MPEA films [66]. Therefore, since each sample in system 1 has a Ti composition >10 at.% (Table 1), perhaps the critical Ti content for the AlCrFeNiTi CCA family has already been reached.

In system 2, the Ti contribution to morphological changes is explored by varying the Ti content between 5 and 35 at.%. Fig. 2 includes the SEM micrographs and diffractograms for samples within system 2, where each row represents a specific Ti composition (5 at.%, 13 at.%, 32 at.%). The SEM figures detail some morphological distinctions between the samples due to compositional differences (see Table 1). The XRD patterns in Fig. 2c, f, and i reveal a phase change due to the varied Ti content, as an increase from 5 at.% to 13 at.% Ti leads to a transition from a body-centered cubic (BCC) structure to an amorphous one. The average crystallite size of the samples varied according to their crystallinity as shown in Table SIII*. Samples with a Ti content greater than 10 at.% feature an amorphous phase in agreement with the observations from system 1. Samples with less than 10 at.% Ti (S2-5Ti-T and S2-5Ti-B) exhibit a crystalline phase, as noted by the XRD patterns in Fig. 2c, where sample S2-5Ti-T display a disordered BCC phase while sample S2-5Ti-B shows an ordered BCC phase with stronger peak intensities. The

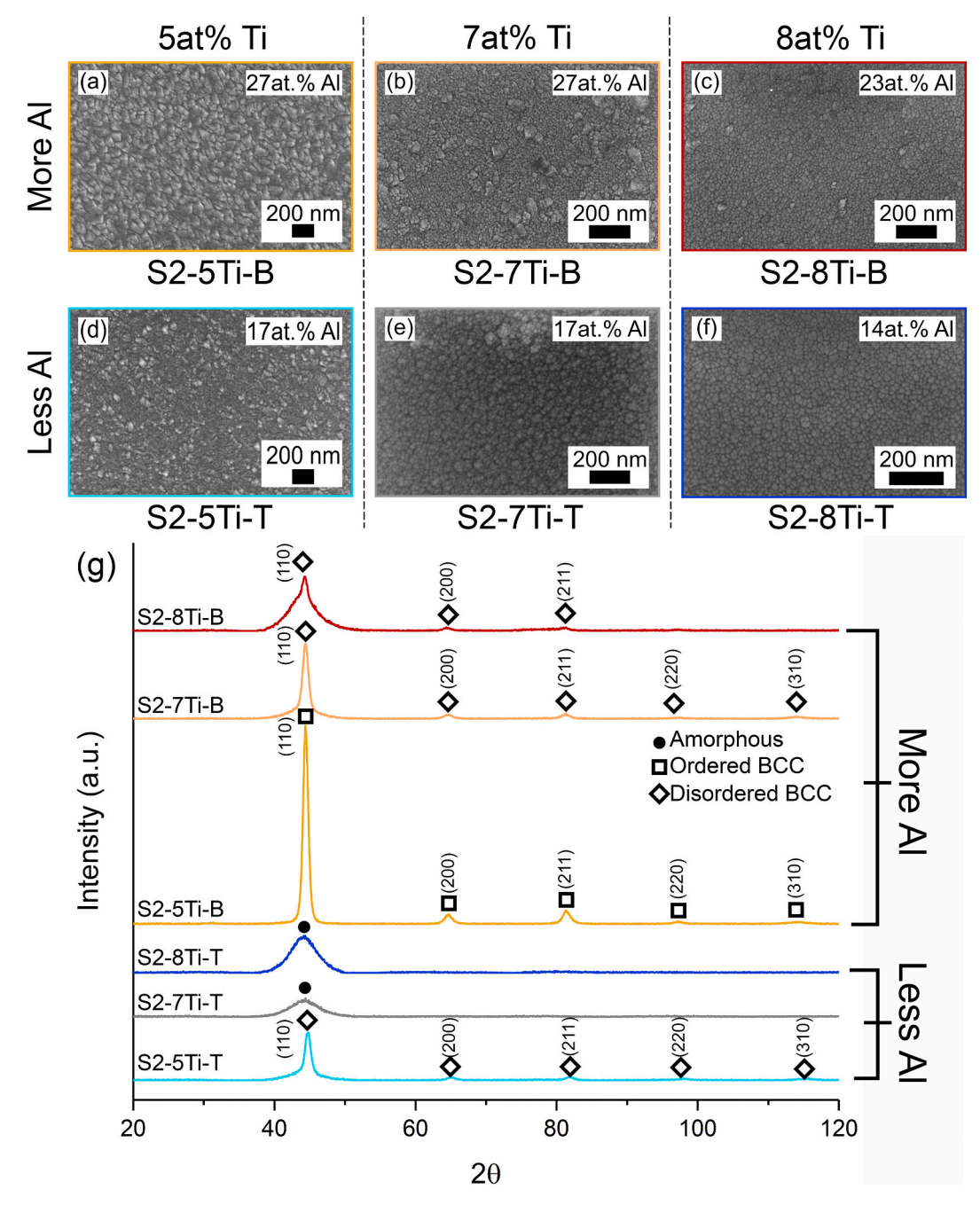


Fig. 3. Top surface SEM micrographs (a – f) and diffractograms (g) for refined samples within system 2. Diffractogram patterns and SEM micrograph borders are color coded by sample. Rows and diffractograms are split amongst samples with either "more" or "less" Al content. Samples with "more" Al content have an Al composition greater than 23 at.%, whereas those with "less" Al content refer to samples with a higher proportion of Cr, Fe, and Ni content in comparison to the Al content. Columns represent a specific Ti content (either 5, 7, or 8 at.%, respectively).

difference between these two samples seems to depend on their respective Al content. In Table 1, it can be seen that sample S2-5Ti-B has a higher Al content than any of the other alloying elements (26.58 at.%), in contrast to S2-5Ti-T, which has 16.60 at.% Al. These results imply that Al does play a role in phase formation, as increased Al content seems to contribute to the degree of crystallinity within these samples.

The findings from systems 1 and 2 suggest the presence of a synergistic relationship between Al and Ti in phase formation that should be further investigated. Therefore, additional samples were synthesized to study the roles of Al and Ti in the composition space below 10 at.% Ti. Fig. 3 includes the top-surface SEM images and XRD patterns for samples within system 2 that are between 5 and 8 at.% Ti. Each column

represents samples with the same Ti content (5 at.%, 7 at.%, 8 at.%). The rows are split amongst samples with "more" Al content, which have an Al composition >23 at.% (Fig. 3a–c), and samples with "less" Al, referring to those with a higher Cr, Fe, and Ni content (Fig. 3d–f). The diffractograms for each sample, included in Fig. 3g, are categorized by Al content as well. As the Ti content is increased from 5 at.% to 7 at.%, the samples with "more" Al content transition from an ordered to a disordered BCC structure. Both peak broadening and a decrease in peak intensity occurred (Fig. 3g), which are indicative of a decrease in nanocrystallite size [67]. Upon comparison of the SEM micrographs in Fig. 3a and b, a decrease in nanocrystallite size from \sim 10 nm to \sim 7 nm (Table SIII) can be observed with an increase in Ti content. As

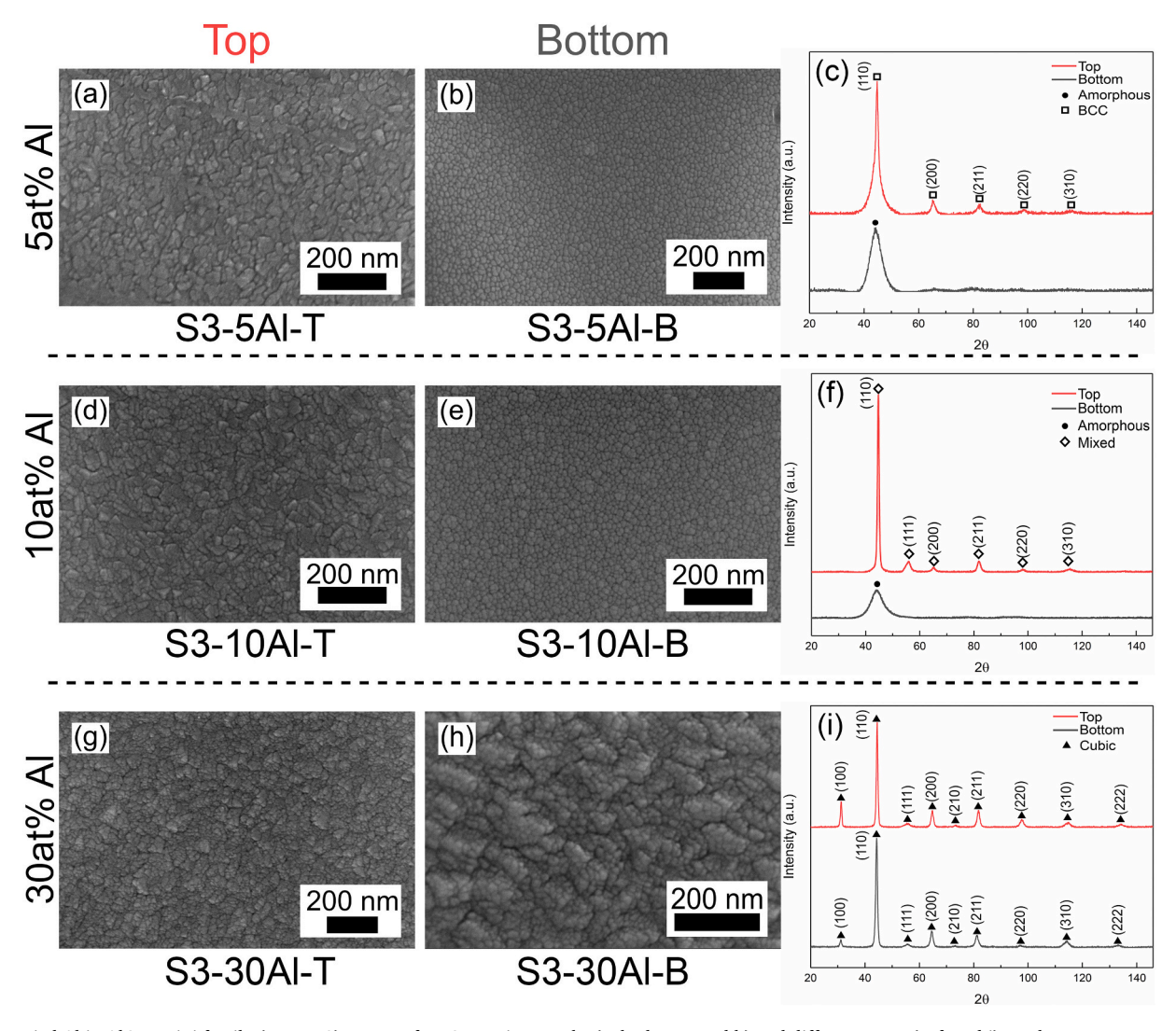


Fig. 4. Varied Al in AlCoFeNiTi family (system 3) - top surface SEM micrographs (a, b, d, e, g, and h) and diffractograms (c, f, and i). Each row represents samples with the same Al content (5 10, and 30 at.% respectively). Columns are split amongst samples that were in either the "top" or "bottom" substrate quadrant position during the sputtering process, while diffractograms are color-coded based on that position.

highlighted in Fig. 3c, a further increase in Ti content to 8 at.% (sample S2-8Ti-B) results in a continued transition to an amorphous structure as further peak broadening and a decrease in nanocrystallite size from \sim 7 nm to \sim 2 nm (Table SIII) are noted in the XRD pattern and SEM micrograph, respectively. In contrast, as Ti is increased from 5 at.% to 7 at.% in samples with "less" Al content, a transition from a disordered BCC structure to an amorphous one occurs (Fig. 3g). It appears that Al plays a role in the degree of crystallinity below a specific Ti content threshold, while amorphous phases begin to form when the amount of Ti exceeds 7 at.%. This finding can explain why the samples within system 1 feature an amorphous phase and no structural alterations regardless of Al content, as each sample within system 1 has a Ti content greater than 7 at.% (Table 1). Thus, the results from systems 1 and 2 further emphasize the synergistic relationship between the two elements.

Prior research on the individual effects of varied Al or Ti content within a given MPEA system provides some key insights on their particular morphological contributions [13,30,31,68–72], although the complex interplay of these two "large" elements found in this work has not been previously addressed. Theoretical [73] and experimental studies have documented that Al additions can lead to a face-centered cubic (FCC) to BCC phase transition in both bulk [3,9,18,42,43,74,75] and film samples [29,56,62,76,77]. This phenomenon has been attributed to a lattice distortion effect, as the close packed FCC lattice must

expand to accommodate the larger Al atoms, thus transitioning to the less closely packed BCC structure [29,56]. However, earlier work on CCA films and coatings suggests that an amorphous phase can be favorable when lattice distortion is high, driven by a large atomic size difference [57,78]. The unique influence of Al is explained by Tang et al., who state that the electronic structure of Al favors covalent bonding with transition metals that have an incompletely filled d-shell, contributing to the formation of crystal structures [79]. The role of Ti on phase formation has also been attributed to lattice distortion effects, as it has caused the formation of heterogeneous and dendritic structures in bulk systems [13,47] and amorphous structures in film systems [66]. In the current work, Al appears to be responsible for the formation of crystal structures and the degree of crystallinity below a critical Ti content of 7 at.% due to its unique valence electron structure. Converesly, increasing the amount of Ti promotes the formation of amorphous phases. In this work, both Al and Ti are considered to be "large" elements as they possess atomic radii greater than 140 pm (146.15 pm for Ti v.s. 143.17 pm for Al [22]). The similarity in their size leads to a complex interplay between the two elements on morphological transformations. The findings here seem to indicate that the elements with the largest atomic radii in a CCA arragment will compete to drive phase evolution, with their valence electron structures contributing to the types of phases formed.

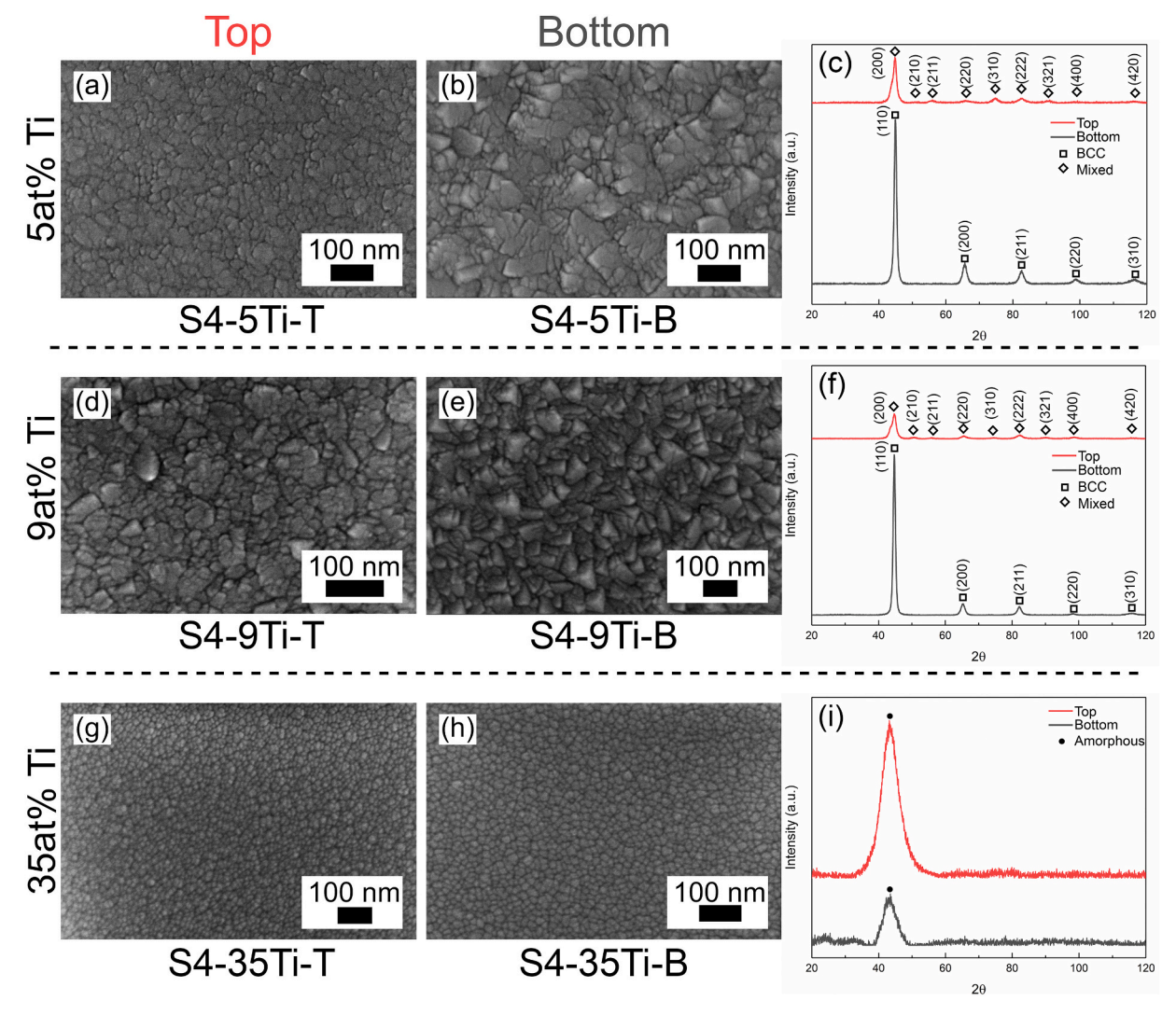


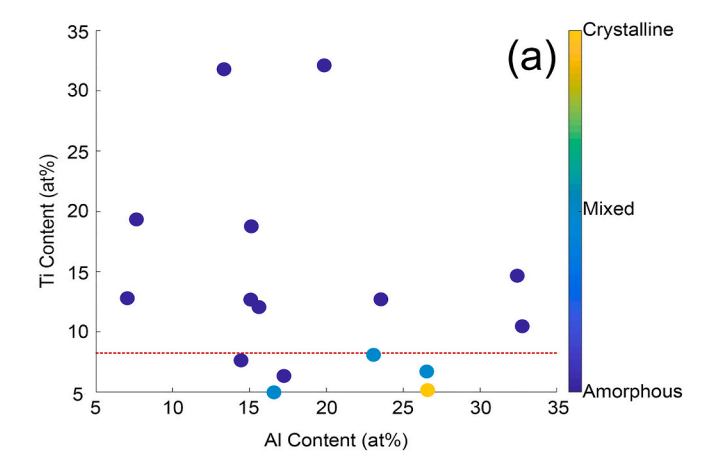
Fig. 5. Varied Ti in AlCoFeNiTi family (system 4) - Top surface SEM micrographs (a, b, d, e, g, and h) and diffractograms (c, f, and i). Each row represents samples with the same Ti content (5, 9, and 35 at.%) respectively. Columns are split amongst samples that were in either the "top" or "bottom" substrate quadrant position during the sputtering process, while diffractograms are color-coded based on that position.

3.2. AlCoFeNiTi – the role of multiple "large" elements influenced by "small" element substitution

To further explore the synergistic interplay of Al and Ti and whether comparable effects translate to other systems, a similar experimental methodology is applied to a different CCA family (AlCoFeNiTi). The overall compositions for system 3 (varied Al) and system 4 (varied Ti) are included in Table 2. The influence of the "small" elements (i.e., transition metals with an atomic radius of <130 pm) on phase formation is also investigated. Specifically, Cr is substituted by similarly sized but structurally dissimilar Co. Both Cr and Co have an atomic radius of approximately 125 pm, but Cr has a BCC structure and a valence electron concentration (VEC) of 6, whereas Co has a VEC of 9, a hexagonal close packed (HCP) structure at room temperature, and an FCC structure at its melting temperature [22].

Top surface SEM micrographs and XRD patterns for the samples within system 3 are presented in Fig. 4, where the rows are separated by specific Al content (5 at.%, 10 at.%, 30 at.%). Fig. 4a–b, in the top row, highlight the samples with 5 at.% Al which feature microstructural distinctions, including a twofold difference in naocrystallite size (Table SIII*), in agreement with the diffractograms in Fig. 4c, which detail a transition from a disordered BCC structure to amorphous. A similar effect is found in the samples with 10 at.% Al (Fig. 4d–e), which

transition from an ordered "mixed" structure to amorphous, as seen by their XRD patterns in Fig. 4f. By contrast, both samples with 30 at.% Al (Fig. 4g-h) display similar microstructural characteristics and an ordered cubic structure as illustrated in Fig. 4i. It is important to note that results from Table 2 indicate that samples with an amorphous phase (S3-5Al-B and S3-10Al-B) have a Ti content greater than 19 at.% while samples below 19 at.% Ti display crystalline structures. Their degree of crystallinity or ordering seems to depend on the Al content (i.e. more Al yields a more ordered crystal structure). The overall results of system 3 have the semblance of the synergistic relationship between Al and Ti found in the AlCrFeNiTi family of CCAs, as each of the samples depict morphological differences due to both Al and Ti content. However, there are two noticeable caveats in the results from system 3: first, there appears to be a higher critical Ti content at which the amorphous phase begins to form, and second, Al does not need to be the dominant element in the alloying arrangement to form ordered phases. For example, as seen in Table 2, sample S3-10Al-T, which only has ~10 at.% Al, still shows an ordered phase in its XRD pattern (Fig. 4i). Thus, it seems that the distinctions in the synergistic relationship between Al and Ti are influenced by the replacement of Cr by Co. These findings are further supported by the results from system 4, which varied Ti content between 5 and 35 at.%. Fig. 5 includes the top surface SEM images and diffractograms for all samples within system 4. Similar to the findings from



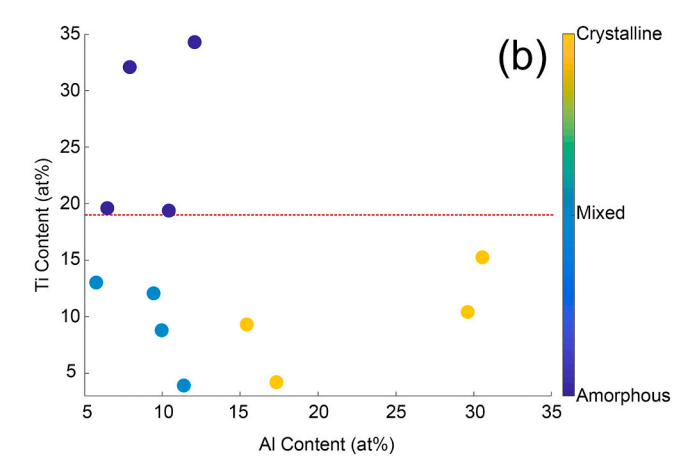


Fig. 6. Crystallography maps of samples in the AlCrFeNiTi (a) and AlCoFeNiTi (b) families of CCAs. Samples are compared by their Al and Ti content and categorized by their respective crystallography: dark blue data points indicate amorphous structures, light blue indicates "mixed" structures, and yellow indicates crystalline structures. The red dotted lines on the y-axes represent the Ti threshold at which amorphous phases begin to form.

system 3, the samples with Ti content values below 19 at.% in system 4 exhibit crystal structures, and the amount of Al content (see Table 2) affects the degree of crystallinity and ordering. This observation is evidenced by the results in the first two rows of Fig. 5 (5 and 9 at.% Ti). Samples in the left column (Fig. 5a and d), which consist of a lower Al content, have a disordered "mixed" phase (Fig. 5c), while samples in the right column (Fig. 5b and e), which contain a higher Al content, exhibit an ordered BCC structure (Fig. 5f). Samples with a Ti content beyond 19 at.% (Fig. 5g–h) depict similar morphologies in their SEM micrographs and show amorphous patterns (Fig. 5i); although, it should be noted that sample S4-35Ti-T does have stronger peak intensities. In systems 3 and 4, ordered crystalline samples feature nanocrystallites that are approximately ten times as large as their amorphous counterparts (Table SIII*). The trends in systems 3 and 4 are consistent with each other, thus emphasizing the influence of the "small" elements on phase formation.

The substitution of Co by Cr has been explored in previous works on bulk MPEAs with relatively consistent results, but there is limited understanding on how this substitution would affect phase formation and synergy in films containing multiple "large" elements. Researchers have found that the addition of Cr and reduction of Co contributes to phase instability and the formation of heterogeneous structures in the $AlCo_xCr_{1-x}FeNi$ quinary family of CCAs [80] and its quarternary derivative alloys AlCoFeNi and AlCrFeNi [81,82]. This effect has been attributed to the assessment that Co minimizes crystallographic mismatch while Cr induces disorder in these types of systems [82].

However, such studies only explored alloying effects in bulk materials and none included Ti in their compositions. In order to visualize the role of Cr and Co on phase formation, Fig. 6 compares the Al and Ti content within the AlCrFeNiTi (Fig. 6a) and AlCoFeNiTi (Fig. 6b) families of CCAs, categorized by crystallographic phase. The data points in dark blue are samples with an amorphous structure, light blue are "mixed" phase samples, and yellow are crystalline samples. The dashed lines on the y-axes indicate the Ti threshold at which amorphous phases form for each CCA family. For the AlCrFeNiTi family the Ti threshold was determined to be approximately 7 at.%, while the AlCoFeNiTi family possessed a threshold of about 19 at.%. It can be observed that the Ti threshold is much lower in samples that contained Cr (Fig. 6a) than those that contained Co (Fig. 6b), and that crystalline phases are more likely to form in the AlCoFeNiTi family than in the AlCrFeNiTi family. Thus, the trends suggest that both the "large" elements and the "small" elements can impact phase formation in these types of systems. These trends and their overall effect on the microstructure can be further verified by measuring the influence of the phase transitions on the mechanical properties, which is discussed in the next section.

3.3. Nanoindentation

Nanoindentation is employed to further understand the complex relationship found between the alloying elements within this work across phase transition zones. Reduced modulus and hardness values for all samples are provided in Table 3. Samples are notated by the following symbols: "●" are amorphous, "♦" are "mixed", and "□" are crystalline. Samples in system 1 with a higher Ti content (see Table 1) yielded lower values of modulus and hardness. In system 2, samples with crystalline or "mixed" phases typically had higher modulus and hardness values than those with amorphous phases, indicating a change in mechanical properties due to phase transitions caused by increased Ti content. Note that sample S2-5Ti-T, which consists of a "mixed" structure, had a slightly higher hardness (7.81 GPa) than sample S2-5Ti-B (7.69 GPa), which was crystalline. These findings are in agreement with a previous review that suggested MPEA films and coatings with amorphous phases will have lower hardness and modulus values than "mixed" or crystalline samples [40]. While in some cases amorphous structures would feature higher hardness values than coarse-grained crystalline structures, nanocrystalline materials have been shown to exhibit superior strength in comparison to their coarse-grained counterparts [83] and amorphous structures alike [84]. In system 3, samples with less Ti content (see Table 2) had hardness values increase by 40% with increasing Al content, which coincides with samples becoming more ordered, but modulus values decreased by 13% in the 5 at.% to 10 at.% Al range and increased by 27% in the 10 at.% to 30 at.% Al range. A similar result had been previously reported by Sun et al. in Al_xCoCr-CuFeNi, where there was an initial decrease in modulus with the addition of Al, followed by an increase in modulus attributed to phase transitions [75]. Amorphous samples in system 3 showed an increase in both modulus and hardness with increasing Al content, however, these samples had lower hardness values than the crystalline or "mixed" samples of this set. In system 4, crystalline samples also exhibited higher hardness and moduli values than "mixed" samples; however, the "mixed" samples had a slightly lower hardness than the amorphous samples.

Overall, the synergistic relationship between Al and Ti contributes to the mechanical properties within the systems studied in this work. Below the critical amount of Ti in both families of alloys, the amount of Al will influence the degree of crystallinity in the samples, thereby affecting the mechanical properties. Non-amorphous samples with "more" Al compared to their counterparts typically had higher modulus (155–170 GPa) and hardness values (7.2–10 GPa) due to ordering. It was also found that additional Ti resulted in a decrease in the mechanical property values (modulus range of 125–155 GPa, hardness range of 6.5–7.3 GPa), as more Ti led to the formation of amorphous phases.

Table 3
Reduced modulus and hardness values determined via nanoindentation. Samples are notated based on their respective crystallography, where "●" indicates an amorphous structure, "◇" indicates a mixed structure, and "□" indicates a crystalline structure.

	AlCrFeNiTi						
System 1 – varied Al			System 2 – varied Ti				
Sample	Reduced modulus (GPa)	Hardness (GPa)	Sample	Reduced modulus (GPa)	Hardness (GPa)		
S1-7Al-T [●]	153.49 ± 3.02	7.08 ± 0.19	S2-5Ti-T [♦]	157.27 ± 4.27	7.81 ± 0.27		
S1-7Al-B [●]	138.72 ± 3.20	6.87 ± 0.18	S2-5Ti-B□	161.60 ± 7.19	7.69 ± 0.50		
S1-15Al-T [●]	148.06 ± 3.45	7.13 ± 0.18	S2-7Ti-T [●]	144.12 ± 4.07	7.34 ± 0.19		
S1-15Al-B [●]	142.71 ± 4.19	6.99 ± 0.19	S2-7Ti-B [♦]	155.64 ± 5.57	7.41 ± 0.31		
S1-33Al-T●	127.62 ± 4.74	7.02 ± 0.23	S2-8Ti-T [●]	155.00 ± 4.27	7.18 ± 0.18		
S1-33Al-B●	139.74 ± 3.80	7.24 ± 0.22	S2-8Ti-B♦	164.34 ± 4.33	7.27 ± 0.20		
			S2-13Ti-T [●]	150.23 ± 4.44	7.24 ± 0.20		
			S2-13Ti-B●	148.00 ± 5.79	7.28 ± 0.23		
			S2-32Ti-T [●]	131.96 ± 3.31	6.80 ± 0.15		
			S2-32Ti-B [●]	140.83 ± 3.01	7.14 ± 0.15		

	AlCoFeNiTi							
System 3 – varied Al			System 4 – varied Ti					
Sample	Reduced modulus (GPa)	Hardness (GPa)	Sample	Reduced modulus (GPa)	Hardness (GPa)			
S3-5Al-T [♦]	152.89 ± 3.55	7.02 ± 0.21	S4-5Ti-T [♦]	154.86 ± 4.56	6.68 ± 0.22			
S3-5Al-B [●]	140.79 ± 2.30	6.71 ± 0.11	S4-5Ti-B□	158.22 ± 6.14	7.18 ± 0.41			
S3-10Al-T [♦]	133.65 ± 4.70	7.47 ± 0.27	S4-9Ti-T [♦]	152.63 ± 3.99	6.99 ± 0.23			
S3-10Al-B [●]	145.66 ± 3.04	7.00 ± 0.16	S4-9Ti-B□	165.44 ± 5.85	7.57 ± 0.31			
S3-30Al-T□	169.78 ± 4.96	9.83 ± 0.33	S4-35Ti-T [●]	139.55 ± 2.62	7.25 ± 0.17			
S3-30Al-B□	164.43 ± 5.90	8.63 ± 0.47	S4-35Ti-B [●]	144.23 ± 2.76	7.21 ± 0.15			

Samples in the current study exhibit hardness and moduli comparable to those of other MPEA systems [33,58,75,85–87], both bulk and film alike, aligning with the expected notable mechanical properties of these types of materials.

4. Conclusions

The results from this study highlight sputtering as a tool to control individual elements within CCA families in order to examine how their atomic characteristics contribute to phase formation and crystallinity. It was found that the "large" elements have a synergistic relationship in which they compete for phase formation, such that a critical threshold exists at which amorphous structures begin to form. The "small" elements can impact this complex interplay, altering the critical threshold and causing different phases to form, as the replacement of Cr by Co changed the crytstalline to amorphous threshold from 7 at.% Ti to 19 at. % Ti. Crystallites were typically an order of magnitude larger in ordered samples than in amorphous samples throughout all systems. Mechanical properties, as derived by nanoindentation, were influenced by these phase changes as well, where amorphous samples generally had lower hardness and moduli than their crystalline or "mixed" phase counterparts. While the results presented in the current work can guide the synthesis of CCA films, it should be noted that these trends may not translate across synthesis methods, particularly due to the high cooling rate of PVD techniques which can mitigate phase separation; therefore further studies are needed to compare how trends translate across synthesis techniques. However, the crystallography maps illustrated in this work may provide a guideline for phase transitions and serve as a model for future alloy design across synthesis methods.

CRediT authorship contribution statement

Daniel C. Goodelman: Conceptualization, Methodology, Formal analysis, Investigation, Writing – original draft, Visualization. Danielle E. White: Formal analysis, Investigation, Writing – review & editing. Andrea M. Hodge: Conceptualization, Writing – review & editing, Visualization, Supervision, Project administration, Funding acquisition.

Declaration of competing interest

The authors declare that they have no known competing financial interests or personal relationships that could have appeared to influence the work reported in this paper.

Acknowledgements

This work was supported by the National Science Foundation [grant number DMR-1709771]. We acknowledge the Core Center of Excellence in Nano Imaging at USC for the use of their SEM and the USC Center of Excellence for Molecular Characterization for the use of their XRD. The authors would like to thank Prof. Dr. Horst Hahn and Dr. Miriam Botros at Karlsruhe Institute of Technology (KIT) for helpful discussions.

Appendix A. Supplementary data

Supplementary data to this article can be found online at https://doi.org/10.1016/j.surfcoat.2021.127651.

References

- O. Senkov, G. Wilks, D. Miracle, C. Chuang, P. Liaw, Refractory high-entropy alloys, Intermetallics 18 (9) (2010) 1758–1765.
- [2] F. Otto, A. Dlouhý, C. Somsen, H. Bei, G. Eggeler, E.P. George, The influences of temperature and microstructure on the tensile properties of a CoCrFeMnNi highentropy alloy, Acta Mater. 61 (15) (2013) 5743–5755.
- [3] C.-J. Tong, M.-R. Chen, J.-W. Yeh, S.-J. Lin, S.-K. Chen, T.-T. Shun, S.-Y. Chang, Mechanical performance of the Al x CoCrCuFeNi high-entropy alloy system with multiprincipal elements, Metall. Mater. Trans. A 36 (5) (2005) 1263–1271.
- [4] Y. Zhao, T. Yang, J. Zhu, D. Chen, Y. Yang, A. Hu, C. Liu, J.-J. Kai, Development of high-strength Co-free high-entropy alloys hardened by nanosized precipitates, Scr. Mater. 148 (2018) 51–55.
- [5] M.A. Hemphill, T. Yuan, G. Wang, J. Yeh, C. Tsai, A. Chuang, P. Liaw, Fatigue behavior of Al0. 5CoCrCuFeNi high entropy alloys, Acta Mater. 60 (16) (2012) 5723–5734.
- [6] Z. Tang, T. Yuan, C.-W. Tsai, J.-W. Yeh, C.D. Lundin, P.K. Liaw, Fatigue behavior of a wrought Al0. 5CoCrCuFeNi two-phase high-entropy alloy, Acta Mater. 99 (2015) 247–258.
- [7] B. Gludovatz, A. Hohenwarter, D. Catoor, E.H. Chang, E.P. George, R.O. Ritchie, A fracture-resistant high-entropy alloy for cryogenic applications, Science 345 (6201) (2014) 1153–1158.

- [8] W.-Y. Ching, S. San, J. Brechtl, R. Sakidja, M. Zhang, P.K. Liaw, Fundamental electronic structure and multiatomic bonding in 13 biocompatible high-entropy alloys, Npj Comput. Mater. 6 (1) (2020) 1–10.
- [9] S.-T. Chen, W.-Y. Tang, Y.-F. Kuo, S.-Y. Chen, C.-H. Tsau, T.-T. Shun, J.-W. Yeh, Microstructure and properties of age-hardenable AlxCrFe1. 5MnNi0. 5 alloys, Mater. Sci. Eng. A 527 (21–22) (2010) 5818–5825.
- [10] C. Liu, H. Wang, S. Zhang, H. Tang, A. Zhang, Microstructure and oxidation behavior of new refractory high entropy alloys, J. Alloys Compd. 583 (2014) 162–169
- [11] M.-R. Chen, S.-J. Lin, J.-W. Yeh, M.-H. Chuang, S.-K. Chen, Y.-S. Huang, Effect of vanadium addition on the microstructure, hardness, and wear resistance of Al 0.5 CoCrCuFeNi high-entropy alloy, Metall. Mater. Trans. A 37 (5) (2006) 1363–1369.
- [12] M.G. Poletti, G. Fiore, F. Gili, D. Mangherini, L. Battezzati, Development of a new high entropy alloy for wear resistance: FeCoCrNiW0. 3 and FeCoCrNiW0. 3+ 5 at. % of C, Mater. Des. 115 (2017) 247–254.
- [13] M. Löbel, T. Lindner, T. Mehner, T. Lampke, Influence of titanium on microstructure, phase formation and wear behaviour of AlCoCrFeNiTix highentropy alloy, Entropy 20 (7) (2018) 505.
- [14] Y. Shi, B. Yang, P. Liaw, Corrosion-resistant high-entropy alloys: a review, Metals 7 (2) (2017).
- [15] Y. Qiu, S. Thomas, M.A. Gibson, H.L. Fraser, N. Birbilis, Corrosion of high entropy alloys, Npj Mater. Degrad. 1 (1) (2017).
- [16] Y. Qiu, M.A. Gibson, H.L. Fraser, N. Birbilis, Corrosion characteristics of high entropy alloys, Mater. Sci. Technol. 31 (10) (2015) 1235–1243.
- [17] Y. Zhang, T.T. Zuo, Z. Tang, M.C. Gao, K.A. Dahmen, P.K. Liaw, Z.P. Lu, Microstructures and properties of high-entropy alloys, Prog. Mater. Sci. 61 (2014) 1–93
- [18] Y.-F. Kao, S.-K. Chen, T.-J. Chen, P.-C. Chu, J.-W. Yeh, S.-J. Lin, Electrical, magnetic, and Hall properties of AlxCoCrFeNi high-entropy alloys, J. Alloys Compd. 509 (5) (2011) 1607–1614.
- [19] P. Koželj, S. Vrtnik, A. Jelen, S. Jazbec, Z. Jagličić, S. Maiti, M. Feuerbacher, W. Steurer, J. Dolinšek, Discovery of a superconducting high-entropy alloy, Phys. Rev. Lett. 113 (10) (2014), 107001.
- [20] Y. Zhang, T. Zuo, Y. Cheng, P.K. Liaw, High-entropy alloys with high saturation magnetization, electrical resistivity and malleability, Sci. Rep. 3 (1) (2013) 1–7.
- [21] C. Chen, H. Zhang, Y. Fan, W. Zhang, R. Wei, T. Wang, T. Zhang, F. Li, A novel ultrafine-grained high entropy alloy with excellent combination of mechanical and soft magnetic properties, J. Magn. Magn. Mater. 502 (2020), 166513.
- [22] D.B. Miracle, O.N. Senkov, A critical review of high entropy alloys and related concepts, Acta Mater. 122 (2017) 448–511.
- [23] A.M. Manzoni, U. Glatzel, New multiphase compositionally complex alloys driven by the high entropy alloy approach, Mater. Charact. 147 (2018) 512–532.
- [24] S. Riva, S.G. Brown, N.P. Lavery, A. Tudball, K.V. Yusenko, Spark plasma sintering of high entropy alloys, in: Spark Plasma Sintering of Materials, Springer, 2019, pp. 517–538.
- [25] M. Vaidya, G.M. Muralikrishna, B.S. Murty, High-entropy alloys by mechanical alloying: a review, J. Mater. Res. 34 (5) (2019) 664–686.
- [26] Y. Zhang, High-entropy Materials vol. 2, Springer Nature Singapore Pte Ltd, 2019, pp. 215–232.
- [27] M.N. Polyakov, T. Chookajorn, M. Mecklenburg, C.A. Schuh, A.M. Hodge, Sputtered Hf-Ti nanostructures: a segregation and high-temperature stability study, Acta Mater. 108 (2016) 8-16.
- [28] M. Moorehead, K. Bertsch, M. Niezgoda, C. Parkin, M. Elbakhshwan, K. Sridharan, C. Zhang, D. Thoma, A. Couet, High-throughput synthesis of Mo-Nb-Ta-W highentropy alloys via additive manufacturing, Mater. Des. 187 (2020), 108358.
- [29] S.A. Kube, S. Sohn, D. Uhl, A. Datye, A. Mehta, J. Schroers, Phase selection motifs in High Entropy Alloys revealed through combinatorial methods: large atomic size difference favors BCC over FCC, Acta Mater. 166 (2019) 677–686.
- [30] S. Wolff-Goodrich, A. Marshal, K.G. Pradeep, G. Dehm, J.M. Schneider, C. H. Liebscher, Combinatorial exploration of B2/L21 precipitation strengthened AlCrFeNiTi compositionally complex alloys, J. Alloys Compd. 853 (2021), 156111.
- [31] Y. Zhang, X. Yan, J. Ma, Z. Lu, Y. Zhao, Compositional gradient films constructed by sputtering in a multicomponent Ti–Al–(Cr, Fe, Ni) system, J. Mater. Res. 33 (19) (2018) 3330–3338.
- [32] C.-Y. Cheng, J.-W. Yeh, High-entropy BNbTaTiZr thin film with excellent thermal stability of amorphous structure and its electrical properties, Mater. Lett. 185 (2016) 456–459.
- [33] J. Cheng, X. Liang, B. Xu, Effect of Nb addition on the structure and mechanical behaviors of CoCrCuFeNi high-entropy alloy coatings, Surf. Coat. Technol. 240 (2014) 184–190.
- [34] K.-H. Cheng, C.-H. Lai, S.-J. Lin, J.-W. Yeh, Structural and mechanical properties of multi-element (AlCrMoTaTiZr) Nx coatings by reactive magnetron sputtering, Thin Solid Films 519 (10) (2011) 3185–3190.
- [35] H.-T. Hsueh, W.-J. Shen, M.-H. Tsai, J.-W. Yeh, Effect of nitrogen content and substrate bias on mechanical and corrosion properties of high-entropy films (AlCrSiTiZr) 100–xNx, Surf. Coat. Technol. 206 (19–20) (2012) 4106–4112.
- [36] P.-K. Huang, J.-W. Yeh, Effects of nitrogen content on structure and mechanical properties of multi-element (AlCrNbSiTiV) N coating, Surf. Coat. Technol. 203 (13) (2009) 1891–1896.
- [37] P.-C. Lin, C.-Y. Cheng, J.-W. Yeh, T.-S. Chin, Soft magnetic properties of high-entropy Fe-Co-Ni-Cr-Al-Si thin films, Entropy 18 (8) (2016) 308.
- [38] W. Sheng, X. Yang, C. Wang, Y. Zhang, Nano-crystallization of high-entropy amorphous NbTiAlSiWxNy films prepared by magnetron sputtering, Entropy 18 (6) (2016) 226.
- [39] L.Z. Medina, L. Riekehr, U. Jansson, Phase formation in magnetron sputtered CrMnFeCoNi high entropy alloy, Surf. Coat. Technol. 403 (2020), 126323.

- [40] W. Li, P. Liu, P.K. Liaw, Microstructures and properties of high-entropy alloy films and coatings: a review, Mater. Res. Lett. 6 (4) (2018) 199–229.
- [41] J.-W. Yeh, S.-J. Lin, M.-H. Tsai, S.-Y. Chang, High-entropy coatings, in: M.C. Gao, et al. (Eds.), High-entropy Alloys: Fundamentals and Applications, Springer International Publishing, Cham, 2016, pp. 469–491.
- [42] H.-P. Chou, Y.-S. Chang, S.-K. Chen, J.-W. Yeh, Microstructure, thermophysical and electrical properties in AlxCoCrFeNi (0≤ x≤ 2) high-entropy alloys, Mater. Sci. Eng. B 163 (3) (2009) 184–189.
- [43] B. Gwalani, S. Gangireddy, S. Shukla, C.J. Yannetta, S.G. Valentin, R.S. Mishra, R. Banerjee, Compositionally graded high entropy alloy with a strong front and ductile back, Mater. Today Commun. 20 (2019), 100602.
- [44] Y. Chen, T. Duval, U. Hung, J. Yeh, H. Shih, Microstructure and electrochemical properties of high entropy alloys—a comparison with type-304 stainless steel, Corros. Sci. 47 (9) (2005) 2257–2279.
- [45] Y.-J. Hsu, W.-C. Chiang, J.-K. Wu, Corrosion behavior of FeCoNiCrCux highentropy alloys in 3.5% sodium chloride solution, Mater. Chem. Phys. 92 (1) (2005) 112–117.
- [46] S. Zhao, Y. Shao, X. Liu, N. Chen, H. Ding, K. Yao, Pseudo-quinary Ti20Zr20Hf20Be20 (Cu20-xNix) high entropy bulk metallic glasses with large glass forming ability, Mater. Des. 87 (2015) 625–631.
- [47] S. Gao, T. Kong, M. Zhang, X. Chen, Y.W. Sui, Y.J. Ren, J.Q. Qi, F.X. Wei, Y.Z. He, Q.K. Meng, Effects of titanium addition on microstructure and mechanical properties of CrFeNiTi x (x = 0.2–0.6) compositionally complex alloys, J. Mater. Res. (2019) 1–10.
- [48] Z.-C. Chang, S.-C. Liang, S. Han, Y.-K. Chen, F.-S. Shieu, Characteristics of TiVCrAlZr multi-element nitride films prepared by reactive sputtering, Nucl. Instrum. Methods Phys. Res., Sect. B 268 (16) (2010) 2504–2509.
- [49] Y. Zhang, C.C. Koch, S.G. Ma, H. Zhang, Y. Pan, Fabrication routes, in: M.C. Gao, et al. (Eds.), High-entropy Alloys: Fundamentals and Applications, Springer International Publishing, Cham, 2016, pp. 151–179.
- [50] P.-K. Huang, J.-W. Yeh, Effects of substrate bias on structure and mechanical properties of (AlCrNbSiTiV) N coatings, J. Phys. D. Appl. Phys. 42 (11) (2009), 115401.
- [51] B. Ren, S. Lv, R. Zhao, Z. Liu, S. Guan, Effect of sputtering parameters on (AlCrMnMoNiZr) N films, Surf. Eng. 30 (2) (2014) 152–158.
- [52] W.-J. Shen, M.-H. Tsai, Y.-S. Chang, J.-W. Yeh, Effects of substrate bias on the structure and mechanical properties of (Al1. 5CrNb0. 5Si0. 5Ti) Nx coatings, Thin Solid Films 520 (19) (2012) 6183–6188.
- [53] R.-S. Yu, C.-J. Huang, R.-H. Huang, C.-H. Sun, F.-S. Shieu, Structure and optoelectronic properties of multi-element oxide thin film, Appl. Surf. Sci. 257 (14) (2011) 6073–6078.
- [54] P.J. Kelly, R.D.J.V. Arnell, Magnetron sputtering: a review of recent developments and applications, Vacuum 56 (3) (2000) 159–172.
- [55] L. Liu, J. Zhu, C. Hou, J. Li, Q. Jiang, Dense and smooth amorphous films of multicomponent FeCoNiCuVZrAl high-entropy alloy deposited by direct current magnetron sputtering, Mater. Des. 46 (2013) 675–679.
- [56] B. Braeckman, F. Boydens, H. Hidalgo, P. Dutheil, M. Jullien, A.-L. Thomann, D. Depla, High entropy alloy thin films deposited by magnetron sputtering of powder targets, Thin Solid Films 580 (2015) 71–76.
- [57] B. Braeckman, D. Depla, Structure formation and properties of sputter deposited Nbx-CoCrCuFeNi high entropy alloy thin films, J. Alloys Compd. 646 (2015) 810–815.
- [58] C. Dang, J.U. Surjadi, L. Gao, Y. Lu, Mechanical properties of nanostructured CoCrFeNiMn high-entropy alloy (HEA) coating, Front. Mater. 5 (2018) 41.
- [59] N.A. Khan, B. Akhavan, H. Zhou, L. Chang, Y. Wang, L. Sun, M.M. Bilek, Z. Liu, High entropy alloy thin films of AlCoCrCu0. 5FeNi with controlled microstructure, Appl. Surf. Sci. 495 (2019), 143560.
- [60] Y.S. Kim, H.J. Park, S.C. Mun, E. Jumaev, S.H. Hong, G. Song, J.T. Kim, Y.K. Park, K.S. Kim, S.I. Jeong, Investigation of structure and mechanical properties of TiZrHfNiCuCo high entropy alloy thin films synthesized by magnetron sputtering, J. Alloys Compd. 797 (2019) 834–841.
- [61] S. Alvi, D.M. Jarzabek, M.G. Kohan, D. Hedman, P. Jenczyk, M.M. Natile, A. Vomiero, F. Akhtar, Synthesis and mechanical characterization of a CuMoTaWV high-entropy film by magnetron sputtering, ACS Appl. Mater. Interfaces 12 (18) (2020) 21070–21079.
- [62] S.K. Bachani, C.-J. Wang, B.-S. Lou, L.-C. Chang, J.-W. Lee, Microstructural characterization, mechanical property and corrosion behavior of VNbMoTaWAI refractory high entropy alloy coatings: effect of Al content, Surf. Coat. Technol. 403 (2020), 126351.
- [63] W. Hume-Rothery, The structure of metals and alloys, Indian J. Phys. 11 (1969) 74.
- [64] B. Cullity, S. Stock, Diffraction III: real samples, in: Elements of X-ray Diffraction, 2001, pp. 174–177.
- [65] Triboindenter Software Version 8.1.1 User Manual, Hysitron Incorporated, Minneapolis, MN, 2007, p. 216.
- [66] Y.-C. Hsu, C.-L. Li, C.-H. Hsueh, Modifications of microstructures and mechanical properties of CoCrFeMnNi high entropy alloy films by adding Ti element, Surf. Coat. Technol. 399 (2020), 126149.
- [67] C.F. Holder, R.E. Schaak, Tutorial on Powder X-Ray Diffraction for Characterizing Nanoscale Materials, ACS Publications, 2019.
- [68] Y. Yu, J. Wang, J. Li, H. Kou, W. Liu, Characterization of BCC phases in AlCoCrFeNiTix high entropy alloys, Mater. Lett. 138 (2015) 78–80.
 [69] Y. Zhao, M. Wang, H. Cui, Y. Zhao, X. Song, Y. Zeng, X. Gao, F. Lu, C. Wang,
- [69] Y. Zhao, M. Wang, H. Cui, Y. Zhao, X. Song, Y. Zeng, X. Gao, F. Lu, C. Wang, Q. Song, Effects of Ti-to-Al ratios on the phases, microstructures, mechanical properties, and corrosion resistance of Al2-xCoCrFeNiTix high-entropy alloys, J. Alloys Compd. 805 (2019) 585–596.

- [70] Y. Qiu, S. Thomas, D. Fabijanic, A. Barlow, H. Fraser, N. Birbilis, Microstructural evolution, electrochemical and corrosion properties of AlxCoCrFeNiTiy high entropy alloys, Mater. Des. 170 (2019), 107698.
- [71] Y. Zhou, Y. Zhang, Y. Wang, G. Chen, Solid solution alloys of Al Co Cr Fe Ni Ti x with excellent room-temperature mechanical properties, Appl. Phys. Lett. 90 (18) (2007) 181904.
- [72] S. Jiang, Z. Lin, H. Xu, Y. Sun, Studies on the microstructure and properties of AlxCoCrFeNiTi1-x high entropy alloys, J. Alloys Compd. 741 (2018) 826–833.
- [73] F. Tian, L. Delczeg, N. Chen, L.K. Varga, J. Shen, L. Vitos, Structural stability of NiCoFeCrAl x high-entropy alloy from ab initio theory, Phys. Rev. B 88 (8) (2013), 085128.
- [74] F. Wang, Y. Zhang, G. Chen, Atomic packing efficiency and phase transition in a high entropy alloy, J. Alloys Compd. 478 (1–2) (2009) 321–324.
- [75] Y. Sun, P. Chen, L. Liu, M. Yan, X. Wu, C. Yu, Z. Liu, Local mechanical properties of AlxCoCrCuFeNi high entropy alloy characterized using nanoindentation, Intermetallics 93 (2018) 85–88.
- [76] T. Borkar, B. Gwalani, D. Choudhuri, C. Mikler, C. Yannetta, X. Chen, R. V. Ramanujan, M. Styles, M. Gibson, R. Banerjee, A combinatorial assessment of AlxCrCuFeNi2 (0< x< 1.5) complex concentrated alloys: microstructure, microhardness, and magnetic properties, Acta Mater. 116 (2016) 63–76.</p>
- [77] V. Dolique, A.-L. Thomann, P. Brault, Y. Tessier, P. Gillon, Complex structure/ composition relationship in thin films of AlCoCrCuFeNi high entropy alloy, Mater. Chem. Phys. 117 (1) (2009) 142–147.
- [78] B. Braeckman, F. Misják, G. Radnóczi, D. Depla, The influence of Ge and in addition on the phase formation of CoCrCuFeNi high-entropy alloy thin films, Thin Solid Films 616 (2016) 703–710.

- [79] Z. Tang, M.C. Gao, H. Diao, T. Yang, J. Liu, T. Zuo, Y. Zhang, Z. Lu, Y. Cheng, Y. Zhang, Aluminum alloying effects on lattice types, microstructures, and mechanical behavior of high-entropy alloys systems, Jom 65 (12) (2013) 1946, 1959.
- [80] T. Borkar, V. Chaudhary, B. Gwalani, D. Choudhuri, C.V. Mikler, V. Soni, T. Alam, R.V. Ramanujan, R. Banerjee, A combinatorial approach for assessing the magnetic properties of high entropy alloys: role of Cr in AlCoxCr1–xFeNi, Adv. Eng. Mater. 19 (8) (2017) 1700048.
- [81] V. Chaudhary, B. Gwalani, V. Soni, R. Ramanujan, R. Banerjee, Influence of Cr substitution and temperature on hierarchical phase decomposition in the AlCoFeNi high entropy alloy, Sci. Rep. 8 (1) (2018) 1–12.
- [82] G. Hillel, L. Natovitz, S. Salhov, S. Haroush, M. Pinkas, L. Meshi, Understanding the role of the constituting elements of the AlCoCrFeNi high entropy alloy through the investigation of quaternary alloys, Metals 10 (10) (2020) 1275.
- [83] C. Suryanarayana, Structure and properties of nanocrystalline materials, Bull. Mater. Sci. 17 (4) (1994) 307–346.
- [84] A.K. Battu, C.V. Ramana, Mechanical properties of nanocrystalline and amorphous gallium oxide thin films, Adv. Eng. Mater. 20 (11) (2018), 1701033.
- [85] X. Feng, G. Tang, M. Sun, X. Ma, L. Wang, K. Yukimura, Structure and properties of multi-targets magnetron sputtered ZrNbTaTiW multi-elements alloy thin films, Surf. Coat. Technol. 228 (2013) \$424–\$427.
- [86] Z. Tang, S. Zhang, R. Cai, Q. Zhou, H. Wang, Designing high entropy alloys with dual fcc and bcc solid-solution phases: structures and mechanical properties, Metall. Mater. Trans. A 50 (4) (2019) 1888–1901.
- [87] S. Fang, C. Wang, C.-L. Li, J.-H. Luan, Z.-B. Jiao, C.-T. Liu, C.-H. Hsueh, Microstructures and mechanical properties of CoCrFeMnNiVx high entropy alloy films, J. Alloys Compd. 820 (2020) 153388.